frontiers | Frontiers in Physics

ORIGINAL RESEARCH
published: 13 June 2022
doi: 10.3389/fphy.2022.945995

MEMS Modulator-Based Mid-Infrared Laser Heterodyne Radiometer for Atmospheric Remote Sensing

Zhengyue Xue[1,2], Fengjiao Shen[3], Jun Li[1,2], Xiaohai Liu[2], Guishi Wang[2], Kun Liu[2], Xiaoming Gao[1,2], Weidong Chen[4] and Tu Tan[2]**

[1]School of Environmental Science and Optoelectronic Technology, University of Science and Technology of China, Hefei, China, [2]Anhui Institute of Optics and Fine Mechanics, Chinese Academy of Sciences, Hefei, China, [3]School of Advanced Manufacturing Engineering, Hefei University, Hefei, China, [4]Laboratoire de Physico-Chimie de l'Atmosphère, Université du Littoral Côte d'Opale, Dunkerque, France

The performance of a mid-infrared laser heterodyne radiometer (MIR-LHR) based on a micro-electro-mechanical system (MEMS) mirror is demonstrated in ground-based solar occultation mode. A MEMS mirror is employed as an alternative modulator to the traditional mechanical chopper. High-resolution (~0.0024 cm^{-1}) transmission spectrum near 3.93 μm was obtained for atmospheric observation of N_2O absorption. Operation of the MIR-LHR with laser-induced shot-noise limited performance was analyzed and experimentally achieved. The laser heterodyne spectrum obtained is consistent with Fourier-transform infrared (FT-IR) spectrometer and atmospheric transmission modeling. Compared to the traditional chopper, the MEMS mirror is smaller, lighter and lower power consumption which makes the system more stable and compact. The reported MIR-LHR in this article has great potential in aircraft instruments and satellite payloads.

Keywords: laser heterodyne radiometer, micro-electro-mechanical system, nitrous oxide, noise analysis, field measurement

OPEN ACCESS

Edited by:
Yufei Ma,
Harbin Institute of Technology, China

Reviewed by:
Shao Jie,
Zhejiang Normal University, China
Chuanliang Li,
Taiyuan University of Science and Technology, China

****Correspondence:***
Tu Tan
tantu@aiofm.ac.cn
Xiaoming Gao
xmgao@aiofm.ac.cn

Specialty section:
This article was submitted to Optics and Photonics, a section of the journal Frontiers in Physics

Received: *17 May 2022*
Accepted: *25 May 2022*
Published: *13 June 2022*

Citation:
Xue Z, Shen F, Li J, Liu X, Wang G, Liu K, Gao X, Chen W and Tan T (2022) MEMS Modulator-Based Mid-Infrared Laser Heterodyne Radiometer for Atmospheric Remote Sensing. Front. Phys. 10:945995. doi: 10.3389/fphy.2022.945995

INTRODUCTION

Long-term continuous observations of greenhouse gases (GHGs) in the atmospheric column are urgently needed to address global climate change and to improve scientific understanding of climate change [1]. At present, several approaches have been proposed and played unique roles in the monitoring of GHGs concentrations, such as satellite remote sensing, LIDAR, and sounding balloons, these approaches are suitable for different fields [2–5]. The detection range of satellite is wide, but the temporal and spatial resolution is low. The detection accuracy of LIDAR is high, however the detection range is limited. The sounding balloon can simultaneously detect a variety of atmospheric parameters and the detection height is up to 30 km, however the cost is high and the path is not uncertain. Laser spectroscopy has been widely used in trace gas detection [6–9]. Ground-based high-resolution Fourier-transform infrared (FT-IR) spectrometers are used to real-time obtain solar spectra and then retrieve vertical concentration profiles of the target GHGs, and the results can also be used for cross-validation of satellite observations [10, 11].

Laser heterodyne radiometer (LHR), which extracts absorption information from a broadband light source (such as the Sun or interstellar medium) by beating it with a narrow-band local oscillator (LO) in a high speed detector, has been widely applied for remote sensing of earth atmosphere and astronomy since the 1970s. Compared to the FT-IR measurement, LHR offers unique advantages

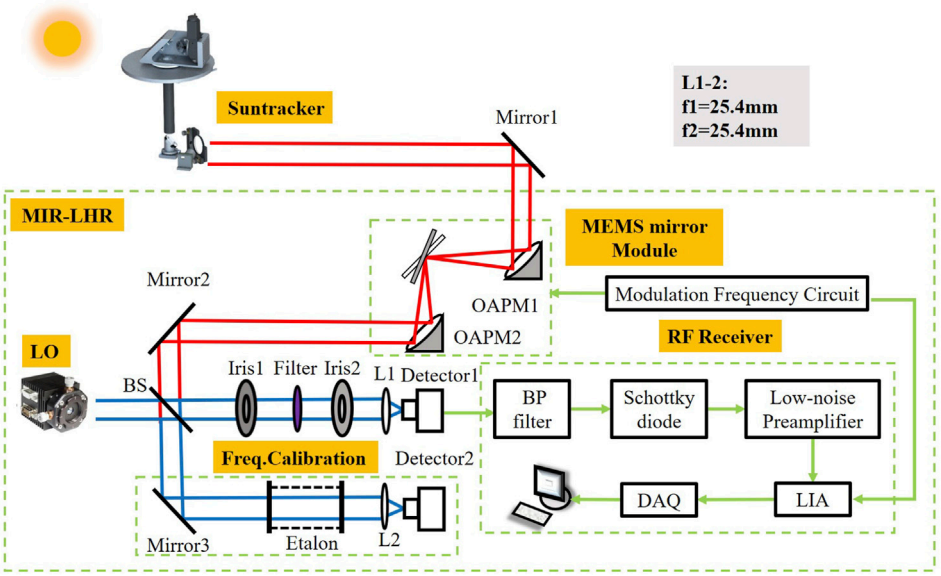

FIGURE 1 | Schematic of the developed MIR-LHR. BS: beam splitter; BP: band-pass; RF: radio frequency; DAQ: data acquisition card; LIA: lock-in amplifier; L: lens; OAPM: off-axis parabolic mirror.

including high spectral resolution, fast response time, small size and high sensitivity. Weidmann *et al.* and Shen *et al.* established mid-infrared (MIR) LHR systems to measure a variety of GHGs, such as CH_4, CO_2, H_2O, O_3 and N_2O in the atmospheric column [12, 13]. Wilson *et al.* and Wang *et al.* developed all-fiber coupled near-infrared (NIR) LHRs for the measurements of CH_4 and CO_2 absorption in the atmospheric column [14, 15]. Robinson et al. demonstrated a hollow waveguide-based miniaturized quantum cascade laser (QCL) heterodyne spectro-radiometer, meanwhile offers an efficient path to miniaturization of the MIR-LHR [16]. In general, sunlight modulation in a LHR system is performed to improve the measurement sensitivity. A mechanical chopper was usually used to realize such modulation. Wang *et al.* and Wilson *et al.* implemented a fiber optical switch to modulate the sunlight which made the LHR more compact and robust [17]. However, the fiber optical switch is only available for application in the near-infrared at the moment.

In this paper, we introduce a micro-electro-mechanical system (MEMS) mirror to modulate the sunlight in a MIR-LHR, which provides many options for the design and development of MIR-LHR. The developed system shows good performance in terms of its spectral resolution and stability. The developed MEMS modulator-based MIR-LHR was validated through measurement of N_2O absorption in the atmospheric column in ground-based solar occultation mode.

EXPERIMENTAL DETAILS

The MIR-LHR developed in the present work is schematically presented in **Figure 1**. A distributed feedback interband cascade laser (DFB-ICL) operating around 3.93 μm at room temperature is used as a LO. It is continuously tunable in frequency from 2,535 cm^{-1} to 2,543 cm^{-1} with the optical output power of more than 15 mW. sunlight containing atmospheric absorption information is captured with a home-made high-precision solar tracker. Solar motion is tracked by photoelectric tracking and proportion-integral-derivative (PID) control with an accuracy of seven arc seconds.

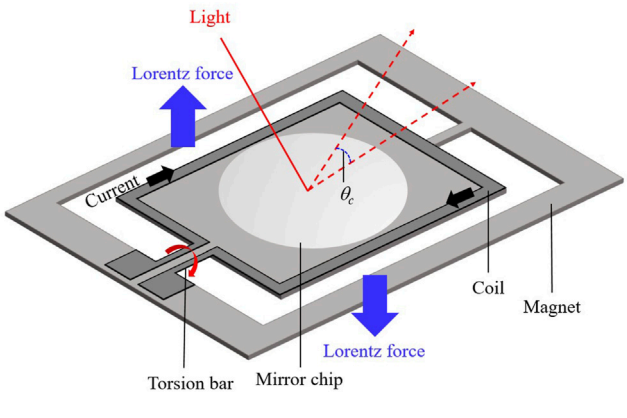

FIGURE 2 | Operation principle of the MEMS mirror.

A MEMS mirror (Hamamatsu, S12237–03P) is used to replace a conventional mechanical chopper to modulate the sunlight. As shown in **Figure 2**, the MEMS mirror is composed of a mirror chip and a magnet that generates a magnetic field. Electrical current passing through the coil produces a Lorentz force under the magnetic field based on Fleming's left-hand rule. This Lorentz force rotates the mirror and the angle of the rotation is proportional to the current injected in the coil. This Lorentz force causes the mirror to rotate at an angle proportional to the

TABLE 1 | Electrical and optical characteristics of the MEMS mirror.

Parameter	Symbol	Range	Unit
Drive current	I_s	±20	mA
Optical reflection angel	θ_s	±18	degrees
Drive frequency	f_s	0–100	Hz
Operating temperature	T_{case}	25 ± 10	C
Resonant frequency	f_{sR}	530 ± 30	Hz

current injected into the coil. The surface of the MEMS mirror is coated with aluminum to ensure high reflectance in the MIR spectral region. The modulation of sunlight is realized by the deflection of MEMS mirror. The MEMS mirror features a large optical reflection angle, high mirror reflectance and low power consumption.

The electrical and optical characteristics of the used MEMS mirror are shown in **Table 1**. In order to minimize the optical noise caused by reflection from other parts of the MEMS mirror, the solar beam size must be smaller than the mirror size (2.6 mm in diameter). According to the divergence angle of the sunlight (~9.2 mrad), a pair of OAPMs (OAPM1and OAPM2) is used to focus and collimate the sunlight to ensure sufficient signal power for the MIR-LHR. The distance between OAPM1 (f_1 = 152.4 mm) and OAPM2 (f_2 = 101.6 mm) is 27.5 cm, and the MEMS mirror is placed at the focal point of OAPM1. The solar power injected into the LHR system is increased by a factor of ~2.5 via collimation and focus of the OAPM pair.

As shown in **Figure 2**, the torsion bar serves as not only an axis of rotation but also a spring for restraining the mirror rotation. The mirror stops rotating and holds an angle when Lorentz force and elastic force of torsion bar spring are equal. The reflection angle and modulation frequency of the MEMS mirror can be adjusted by changing the amplitude and frequency of current in the coil, respectively. The theoretical optical reflection angle θ_c is expressed as follows [18, 19]:

$$\theta_c(t) = A_c * sin(2\pi f_s * t) \quad (1)$$

where A_c is the amplitude of the current flowing in the coil.

The actual optical reflection angle θ_s, affected by the temperature coefficient, can be expressed as:

$$\theta_s(I_s(t)) = \theta_c(t) + d\theta_s \quad (2)$$

where

$$I_s(t) = \sum_{n=0}^{m}\left[a(m,n) * \left\{A_c\left(1 - \left(\frac{f_s}{f_{sR}}\right)^2\right) * sin(2\pi f_s t + \phi)\right\}\right] \quad (3)$$

where *a(m, n)* is the correction factor, m is the order, ϕ is the phase, and the influence of the phase in the phase-locked demodulation is negligible [20].

Since resonance occurs when the mirror exhibits square wave motion, it is important to set the period of the square wave as close as possible to the integer multiple of the resonant frequency's reciprocal [21]. The characteristic resonant frequency of the used MEMS mirror is approximately 530 Hz in the operating temperature range of 25 ± 10°C.

The sunlight collected by the solar tracker is shaped and modulated by the MEMS modulator module, the modulation frequency and duty cycle of the MEMS mirror can be adjusted through its drive current (The duty cycle used in this study is fixed at 50%). The beam splitter is adopted as a mixing device to combine the modulated solar beam with the LO light beam from the ICL. The combined beams are filtered by an optical filter (with a FWHM (full width at half maximum) of 100 nm centered at 3.94 μm) and focused on the photomixer (Detector 1: PV-2TE-4, VIGO System S. A.). A small fraction of the ICL beam reflected through BS is used for frequency calibration, a germanium etalon (with a free spectral range of ~0.0246 cm^{-1}) followed by Detector two is applied for relative frequency metrology. The intermediate frequency (IF) signal at radio frequency (RF) from the AC output of the photomixer is filtered with a band-pass filter and converted into a DC signal by a Schottky diode (HEROTEK, DHM080BB). The IF signal is then amplified by a low-noise preamplifier (SR560, Stanford Research Systems) with a gain of 60 dB. The amplified IF signal is demodulated using a LIA (Standford, SRS850) at the modulation frequency of the MEMS mirror and is then acquired by a DAQ card (USB-6210, NI Inc.) at a sampling rate of 500 kHz via a LabVIEW-based program. The DC output of the photomixer for monitoring the ICL power is acquired by the DAQ card.

INSTRUMENT PERFORMANCE

In order to obtain the best signal-to-noise ratio (SNR), modulating frequency of the MEMS mirror was investigated. **Figure 3** shows the square wave responses of sunlight modulated by the MEMS mirror at different frequencies. The high-frequency oscillation is suppressed when the drive frequency f_s is 5.3 Hz **Figure 3A**, and the corresponding period (~0.188,679 s) is close to the integer multiple of the characteristic resonant frequency's reciprocal (~0.00188,679 s). When the drive frequency f_s is 8 Hz **Figure 3B**, the oscillation occurs, as shown in the inset of **Figure 3B**, and it takes time to stabilize the given optical reflection angle depending on the drive current I_s. Therefore, the modulation frequency of 5.3 Hz, which can reduce the influence of the oscillation of the MEMS mirror on the modulation, was selected for the further MIR-LHR measurements.

Due to the narrow linewidth of the ICL [~megahertz (MHz)], the spectral resolution of the LHR is usually determined by the electronic bandwidth of the band-pass filter. Subsequently, an appropriate band-pass filter was selected by analyzing the spectrum of heterodyne signal and background noise via a RF signal analyzer (Agilent Technologies, N9000A), as shown in **Figure 4**, As can be seen, several noise peaks appear in the regions from 10 to 40 MHz and 80–120 MHz, respectively (**Figure 4** in blue), which may significantly impact the LHR performance. Therefore, a filter with a pass-band of 45–81 MHz, which has low noise, was applied for LHR measurement. The selected pass-band results in a double-sideband spectral resolution of 72 MHz (0.0024 cm^{-1}).

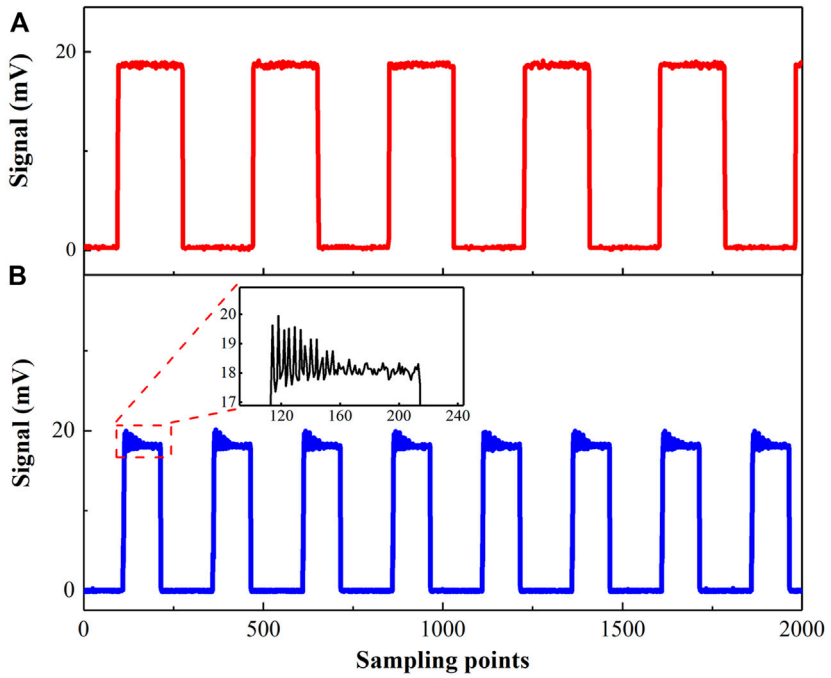

FIGURE 3 | Square wave responses at **(A)** 5.3 Hz; **(B)** 8 Hz, the inset: high-frequency oscillation features.

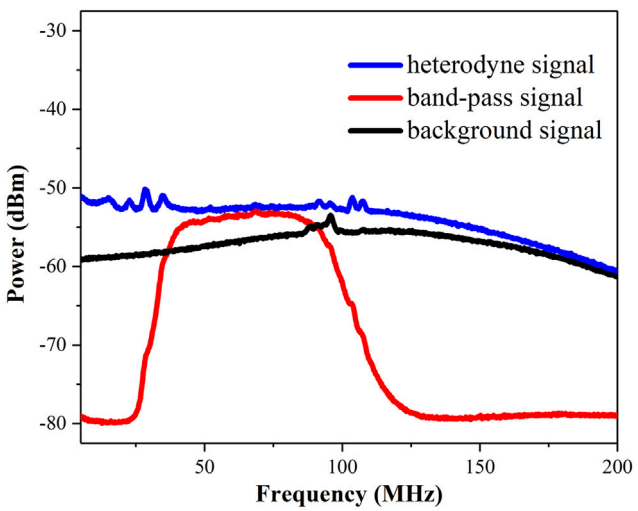

FIGURE 4 | Spectral analysis of heterodyne signal (*blue curve*); band-pass signal (*red curve*) and background signal (*black curve*).

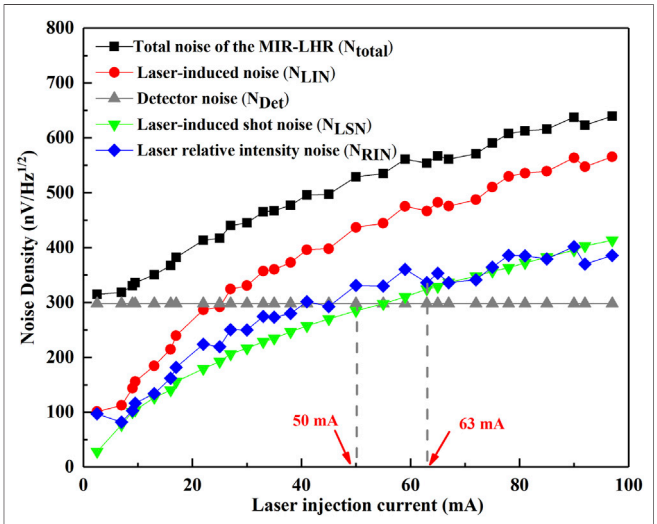

FIGURE 5 | Plots of measured system total noise density, laser-induced noise density, detection noise density, laser-induced shot noise density, and laser relative intensity noise density versus LO injection current, respectively.

As LO power is usually much larger than the incident sunlight power, the sunlight power induced noise can be rendered negligible in practical application, and the main dominant sources in a LHR receiver are detection noise, laser-induced noise, sunlight-induced noise [22]. The sunlight-induced noise can be rendered negligible because LO power is usually much larger than sunlight power. In order to obtain the optimal LO power range (as a linear function of the LO injection current) of the LHR system, it is necessary to analyze noise sources at different LO injection current. The total noise densities N_{total} from the RF output of the VIGO detector within a RF filter pass-band of 45–81 MHz were measured at different LO photocurrents using the signal analyzer, as plotted in **Figure 5** (*black square*). The total noise density N_{total} (nV/Hz$^{1/2}$) of a LHR system can be expressed by [22, 23]:

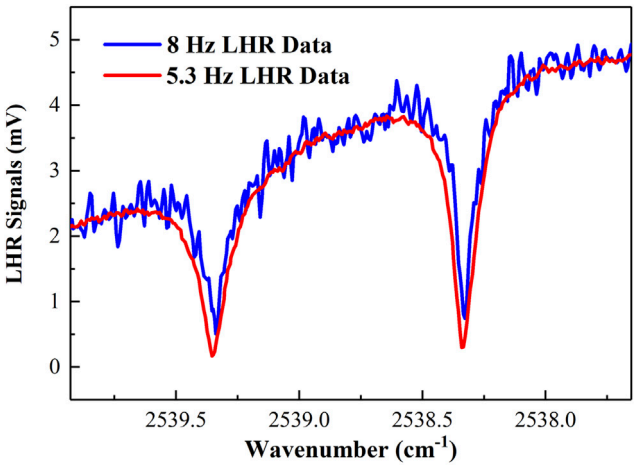

FIGURE 6 | Raw heterodyne signals at 5.3 Hz (*red curve*) and 8 Hz (*blue curve*) modulation frequencies, LO wavelength as a function of the injection current.

$$N_{\text{total}} = \sqrt{N_{Det}^2 + N_{LIN}^2} \tag{4}$$

and

$$N_{LIN}^2 = N_{LSN}^2 + N_{RIN}^2 \tag{5}$$

where N_{Det} was directly measured at the RF output of the VIGO detector without light incidence including the background noise, the Johnson noise, and the dark noise. N_{LIN} is the total laser-induced noise density, including laser-induced shot-noise N_{LSN} and laser relative intensity noise N_{RIN}.

Given the detection noise N_{Det} of 297 nV/Hz$^{1/2}$ (**Figure 5**, *gray triangle*) measured without LO light and the resolution bandwidth (RBW) is 1 MHz. The laser-induced noise density N_{LIN} (**Figure 5**, *red circle*) is obtained by subtracting the detection noise N_{Det} from the measured total noise density N_{total} based on **Eq 4**. The laser-induced shot-noise density N_{LSN} (**Figure 5**, *green triangle*) was calculated by [24]:

$$N_{LSN} = R_{ti} \cdot \sqrt{2 \cdot e \cdot I_{dc}} \tag{6}$$

with R_{ti} = 2200 V/A the transimpedance of the photomixer and I_{dc} is the LO injection current as a linear function of LO power. The laser relative intensity noise N_{RIN} is obtained by subtracting the laser-induced shot-noise density N_{LSN} from the laser-induced noise density N_{LIN} based on **Eq 5**. As shown in **Figure 5**, at LO injection current I_{dc} < 63 mA, the laser relative intensity noise N_{RIN} is larger than the laser-induced shot-noise density N_{LSN}. And at LO njection current >63 mA, the laser relative intensity noise N_{RIN} is approximately equal to the laser-induced shot-noise density N_{LSN}, and they are both larger than the detection noise N_{Det}. At LO injection current I_{dc} > 50 mA, N_{LSN} is larger than N_{Det}. Meanwhile, the maximum current tuning range of the LO (ICL) laser is 0–100 mA. Therefore, the optimal LO injection current I_{dc} of the LHR system should be in the range of 63–100 mA.

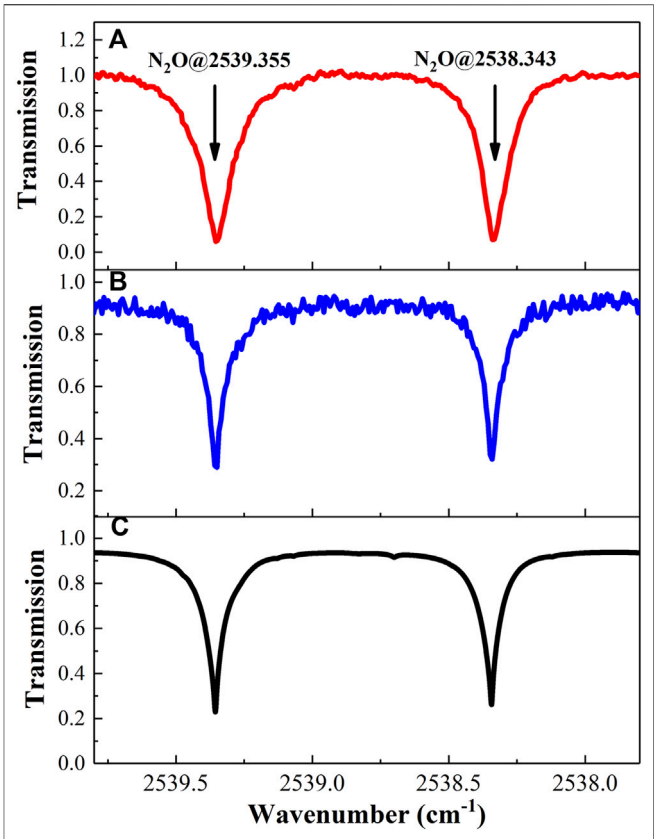

FIGURE 7 | (A) LHR spectrum, **(B)** FT-IR spectrum, and **(C)** atmospheric transmission modelling spectrum of N_2O in the atmospheric column.

FIELD RESULTS

LHR measurements have been performed in Hefei (31.9°N/117.166°E, 40 m above sea level) in China at 15:00 on 10 November 2021. The LO frequency was tuned from 2,537.552 cm^{-1} to 2,539.828 cm^{-1} via the current tuning in point-by-point mode with a current step of 0.1 mA, to detect two N_2O absorption lines at 2,538.343 cm^{-1} and 2,539.355 cm^{-1}, respectively. The LHR signals at MEMS modulation frequencies of 5.3 Hz (*red curve*) and 8 Hz (*blue curve*) are shown in **Figure 6**, where the LHR signal at 5.3 Hz modulation frequency exhibits higher SNR. **Figure 6** shows a calibration curve of the laser wavelength as a function of the laser current at temperature of 16°C.

The absorption spectrum of N_2O in the atmospheric column measured by the MIR-LHR system is shown in **Figure 7A**, accompanied a FT-IR spectrum **Figure 7B** measured with a Bruker IFS 125HR Fourier-transform spectrometer (FTS) (resolution: 0.02 cm^{-1}) recorded at the same location and same time. A calculated spectrum from the atmospheric transmission modeling is given as well in **Figure 7C**.

As expected, the LHR spectrum based on the MEMS mirror modulator is basically consistent with the two reference spectra. Since the laboratory is located in the middle of the round island,

affected by the interference of geographical position, water vapor absorption and absorption path (solar zenith angle), the line-shape and absorption depth of the LHR spectrum are slightly different from the two reference spectra [25]. Compared with FT-IR spectrum, LHR spectrum shows a higher SNR. Moreover, compared with traditional choppers, the MEMS modulator allows for a more compact, stable and versatile MIR-LHR because of its small size ($32.3 \times 32.3 \times 20\ mm^3$ vs $90 \times 120 \times 70\ mm^3$), light weight (0.1 vs 2 kg) and low power consumption (0.2 vs 20 W). It is worthwhile to note that the MEMS mirror can achieve simultaneous measurement of multi-channel and multi-band laser heterodyne spectra those cannot be achieved by traditional choppers, which expands the application of MIR-LHR in the field of atmospheric detection.

CONCLUSION

In conclusion, a MIR-LHR system using a MEMS mirror modulator was developed. The modulation frequencies of MEMS modulator-based MIR-LHR were experimentally investigated. The contributions of main noise sources in the LHR system were quantitatively analyzed. N_2O absorption in the atmospheric column was measured by the developed MIR-LHR system in the ground-based solar occultation mode. The measured LHR spectrum was consistent with the FT-IR spectrum and the atmospheric transmission modeling. Lighter, smaller and lower power consumption MEMS mirror has greatly improved the volume and stability of MIR-LHR, which makes MIR-LHR very suitable, not only for ground-based but also for aircraft- and satellite-based measurements.

DATA AVAILABILITY STATEMENT

The raw data supporting the conclusion of this article will be made available by the authors, without undue reservation.

AUTHOR CONTRIBUTIONS

ZX was responsible for the overall design and implementation of the experiment, data processing, and manuscript writing. TT and GW provided inspiration for the theory and operation of the experiment and suggestions for the revision of manuscripts. JL and XL provided help for the construction of the experimental device and data collection. WC and FS provided writing reviewing and editing. XG and KL: Supervision, Funding acquisition.

FUNDING

Key Project of the National Natural Science Foundation of China (41730103) and National Natural Science Foundation of China (41405022, 42075128).

REFERENCES

1. Deutscher NM, Griffith DWT, Bryant GW, Wennberg PO, Toon GC, Washenfelder RA, et al. Total Column CO₂ Measurements at Darwin, Australia - Site Description and Calibration against *In Situ* Aircraft Profiles. *Atmos Meas Tech* (2010) 3:947–58. doi:10.5194/amt-3-947-2010
2. Chan KL, Valks P, Slijkhuis S, Köhler C, Loyola D. Total Column Water Vapor Retrieval for Global Ozone Monitoring Experience-2 (GOME-2) Visible Blue Observations. *Atmos Meas Tech* (2020) 13:4169–93. doi:10.5194/amt-13-4169-2020
3. Lange D, Behrendt A, Wulfmeyer V. Compact Operational Tropospheric Water Vapor and Temperature Raman Lidar with Turbulence Resolution. *Geophys Res Lett* (2019) 46:14844–53. doi:10.1029/2019gl085774
4. Brunamonti S, Jorge T, Oelsner P, Hanumanthu S, Singh BB, Kumar KR, et al. Balloon-borne Measurements of Temperature, Water Vapor, Ozone and Aerosol Backscatter on the Southern Slopes of the Himalayas during StratoClim 2016-2017. *Atmos Chem Phys* (2018) 18:15937–57. doi:10.5194/acp-18-15937-2018
5. Ren H, Li A, Hu Z, Huang Y, Li X. Measurement of Atmospheric Water Vapor Vertical Column Concentration and Vertical Distribution in Qingdao Using Multi-axis Differential Optical Absorption Spectroscopy. *Acta Phys Sin* (2020) 69:204–6. doi:10.7498/aps.69.20200588
6. Ma Y, He Y, Tong Y, Yu X, Tittel FK. Quartz-tuning-fork Enhanced Photothermal Spectroscopy for Ultra-high Sensitive Trace Gas Detection. *Opt Express* (2018) 26:32103–10. doi:10.1364/oe.26.032103
7. Lang Z, Qiao S, Ma Y. Acoustic Microresonator Based In-Plane Quartz-Enhanced Photoacoustic Spectroscopy Sensor with a Line Interaction Mode. *Opt Lett* (2022) 47:1295–8. doi:10.1364/ol.452085
8. Li C, Shao L, Meng H, Wei J, Qiu X, He Q, et al. High-speed Multi-Pass Tunable Diode Laser Absorption Spectrometer Based on Frequency-Modulation Spectroscopy. *Opt Express* (2018) 26:29330–9. doi:10.1364/oe.26.029330
9. Ma Y, Feng W, Qiao S, Zhao Z, Gao S, Wang Y. Hollow-core Anti-resonant Fiber Based Light-Induced Thermoelastic Spectroscopy for Gas Sensing. *Opt Express* (2022) 30:18836–44. doi:10.1364/oe.460134
10. Pidwirny M. *Fundamentals of Physical Geography*. 2nd ed.. New Delhi: Cengage Learning (2006).
11. Tsai T. *External Cavity Quantum cascade Lasers for Spectroscopic Applications*. Princeton: Princeton University (2012). PhD Thesis
12. Tsai TR, Rose RA, Weidmann D, Wysocki G. Atmospheric Vertical Profiles of O3, N2O, CH4, CCl2F2, and H2O Retrieved from External-Cavity Quantum-cascade Laser Heterodyne Radiometer Measurements. *Appl Opt* (2012) 51:8779–92. doi:10.1364/ao.51.008779
13. Shen F, Wang G, Wang J, Tan T, Wang G, Jeseck P, et al. Transportable Mid-infrared Laser Heterodyne Radiometer Operating in the Shot-Noise Dominated Regime. *Opt Lett* (2021) 46:3171. doi:10.1364/ol.426432
14. Wilson EL, DiGregorio AJ, Villanueva G, Grunberg CE, Souders Z, Miletti KM, et al. A Portable Miniaturized Laser Heterodyne Radiometer (Mini-LHR) for Remote Measurements of Column CH_4 and CO_2. *Appl Phys B* (2019) 125:211. doi:10.1007/s00340-019-7315-8
15. Wang J, Sun C, Wang G, Zou M, Tan T, Liu K, et al. A Fibered Near-Infrared Laser Heterodyne Radiometer for Simultaneous Remote Sensing of Atmospheric CO_2 and CH_4. *Opt Lasers Eng* (2020) 129:106083. doi:10.1016/j.optlaseng.2020.106083
16. Robinson I, Butcher HL, Macleod NA, Weidmann D. Hollow Waveguide-Miniaturized Quantum cascade Laser Heterodyne Spectro-Radiometer. *Opt Express* (2021) 29:2299. doi:10.1364/oe.415371
17. Wang J, Wang G, Tan T, Zhu G, Sun C, Cao Z, et al. Mid-infrared Laser Heterodyne Radiometer (LHR) Based on a 3.53 μm Room-Temperature Interband cascade Laser. *Opt Express* (2019) 27:9610–9. doi:10.1364/OE.27.009610

18. Xue C, Zheng L, Zhang W, Zhang B, Jian A. A Dynamic Stress Analyzer for Microelectromechanical Systems (MEMS) Based on Raman Spectroscopy. *Raman Spectrosc* (2007) 4:38. doi:10.1002/jrs.1673
19. Ma X, Kuo GS. Optical Switching Technology Comparison: Optical MEMS vs. Other Technologies. *IEEE Commun Mag* (2003) 41:S23. doi:10.1109/mcom.2003.1244924
20. Pomeroy JW, Gkotsis P, Zhu M, Leighton G, Kirby P, Kuball M. Dynamic Operational Stress Measurement of MEMS Using Time-Resolved Raman Spectroscopy. *Microelectromech Syst* (2008) 17:1321. doi:10.1109/jmems.2008.2004849
21. Serrano JR, Kearney SP. Time-Resolved Micro-raman Thermometry for Microsystems in Motion. *Heat Transf* (2008) 130:122401. doi:10.1115/1.2976552
22. Wang Y, Nikodem M, Wysocki G. Cryogen-free Heterodyne-Enhanced Mid-infrared Faraday Rotation Spectrometer. *Opt Express* (2013) 21:740. doi:10.1364/oe.21.000740
23. Blaney TG. Signal-to-noise Ratio and Other Characteristics of Heterodyne Radiation Receivers. *Space Sci Rev* (1975) 17:691–702. doi:10.1007/bf00727583
24. Klimchuk AY, Nadezhdinskii AI, Ponurovskii YY, Shapovalov YP, Rodin AV. On the Possibility of Designing a High-Resolution Heterodyne Spectrometer for Near-IR Range on the Basis of a Tunable Diode Laser. *Quan Electron* (2012) 42:3. doi:10.1070/qe2012v042n03abeh014759
25. Kämpfer N. *Monitoring Atmospheric Water Vapor*. New York, NY: Springer (2013).

Conflict of Interest: The authors declare that the research was conducted in the absence of any commercial or financial relationships that could be construed as a potential conflict of interest.

Publisher's Note: All claims expressed in this article are solely those of the authors and do not necessarily represent those of their affiliated organizations, or those of the publisher, the editors and the reviewers. Any product that may be evaluated in this article, or claim that may be made by its manufacturer, is not guaranteed or endorsed by the publisher.